J Adv Ceram

Research Article

La-doped $Bi_4Ti_3O_{12}$ nanosheets: Ferroelectric polarization-enhanced carrier dynamics for efficient tetracycline photodegradation

Yi Xu[1,†], Guoping Wang[2,†], Bingbing Yang[3,✉], Yitong Li[1], Le Chen[1], Ruibin Wang[1], Hongqing Wang[1,✉], Linghua Jin[1,✉]

Cite this article: Xu Y, Wang G, Yang B, et al. *J Adv Ceram* 2026, **15**(3): 9221248. https://doi.org/10.26599/JAC.2026.9221248

ABSTRACT: The development of high-performance photocatalysts is crucial for the efficient photodegradation of antibiotics. A key challenge in photocatalysis is charge recombination, which occurs both within the bulk and at the surface of semiconductor catalysts. In this study, charge recombination was suppressed by enhancing carrier dynamics through ferroelectric polarization in $Bi_4Ti_3O_{12}$ (BTO)-based materials, leading to a significant improvement in tetracycline (TC) degradation performance. Our results demonstrate that La doping strengthens ferroelectric polarization, improving charge carrier dynamics and emphasizing the critical role of polarization in photocatalysis. Differences in polarization led to varying effects on charge carrier dynamics, which directly influenced the photocatalytic degradation of TC. La-doped BTO (La-BTO) exhibited the highest photocurrent density, the lowest charge transfer resistance, and a reduced photoluminescence (PL) lifetime when compared with both pristine and depolarized BTO. Photocatalytic tests revealed that La-BTO achieved nearly complete TC degradation within 30 min under light irradiation, with $\cdot O_2^-$ and ·OH radicals identified as the primary oxidative species. Specifically, La-BTO achieved a 94.6% degradation rate, which is significantly higher than that of undoped BTO (70.7%) and depolarized BTO (40.7%). These findings demonstrate that polarization-driven carrier dynamics are crucial for optimizing photocatalytic antibiotic degradation, offering new insights into the rational design of high-performance photocatalysts for water purification.

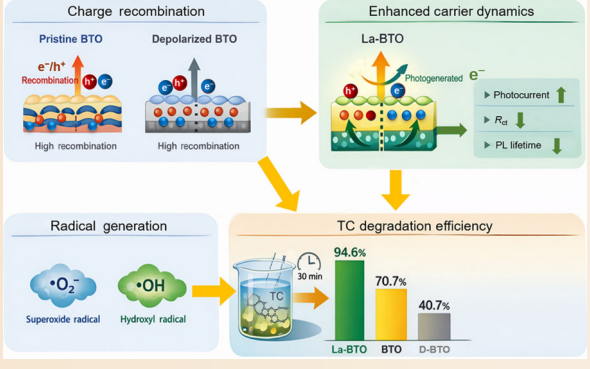

KEYWORDS: ferroelectric polarization; photocatalysis; La-doped $Bi_4Ti_3O_{12}$ (La-BTO); tetracycline degradation

1 Introduction

The widespread occurrence of pharmaceutical contaminants in aquatic environments has emerged as a pressing environmental and public health concern [1,2]. Among these pollutants, antibiotics are particularly problematic due to their chemical persistence, biological activity, and disruptive effects on microbial ecosystems [3–5]. Tetracycline (TC), a widely used antibiotic in human medicine, veterinary practice, and animal husbandry, has been frequently detected in various aquatic environments. Due to its incomplete absorption and metabolism, a substantial fraction of TC is excreted in unmetabolized or partially metabolized forms, eventually entering municipal wastewater, agricultural runoff, and natural aquatic systems [6–8]. Consequently, TC residues have been detected in surface water, groundwater, sediments, and even drinking water sources worldwide. Its high environmental persistence, combined with bioaccumulation and ecotoxicity, poses severe risks to aquatic ecosystems [9–11]. More alarmingly, prolonged exposure to sublethal concentrations of TC contributes to the emergence and spread of antibiotic-resistant bacteria and resistance genes, thereby diminishing the effectiveness of antibiotic therapies and threatening global health [12].

Given these risks, the efficient and sustainable removal of TC from aqueous environments is an urgent priority [13–15]. Among available remediation strategies, semiconductor-based photocatalysis has attracted considerable attention as a green and effective technology [16,17]. This approach utilizes light irradiation (ultraviolet (UV) or visible (Vis)) to activate

† Yi Xu and Guoping Wang contributed equally to this work.

[1] School of Chemistry and Chemical Engineering, University of South China, Hengyang 421001, China. [2] Guang'an Institute of Technology, Guang'an 638000, China. [3] Key Laboratory of Materials Physics, Institute of Solid State Physics, HFIPS, Chinese Academy of Sciences, Hefei 230031, China.

✉ Corresponding authors. E-mail: B. Yang, bbyang@issp.ac.cn; H. Wang, hqwang2015@126.com; L. Jin, jinlh@usc.edu.cn

Received: September 26, 2025; Revised: November 8, 2025; Accepted: January 11, 2026

semiconductors, generating electron–hole (e^-–h^+) pairs that drive redox reactions and mineralize organic pollutants. Conventional photocatalysts such as TiO_2, g-C_3N_4, and $BiVO_4$ have been widely studied for TC degradation [18–31]. However, their practical utility remains limited by rapid e^-–h^+ recombination, narrow light absorption ranges, and relatively low efficiencies. To overcome these issues, various strategies, such as elemental doping [32,33], heterojunction construction [18,19,22,23,29], and defect or surface engineering [25,34,35], have been developed. Most of these approaches rely on band structure modulation, which can improve light absorption and redox capability. Nevertheless, such extrinsic modifications often yield only incremental performance improvements and are hindered by poor long-term stability due to insufficient carrier separation and compromised carrier dynamics.

In contrast, ferroelectric polarization offers an intrinsic and sustainable driving force for enhancing photocatalytic activity [36–38]. Ferroelectric materials possess spontaneous polarization, producing strong internal electric fields that promote spatial separation and directional migration of photogenerated carriers [39–41]. This intrinsic polarization not only facilitates charge separation in the bulk but also maintains stability under continuous illumination, thereby enhancing photocatalytic performance without requiring sacrificial agents or cocatalysts [42–44]. As such, ferroelectric polarization emerges as a critical factor in governing charge dynamics and photocatalytic performance. Among ferroelectric materials, $Bi_4Ti_3O_{12}$ (BTO) has received considerable attention due to its Aurivillius-type layered structure, robust ferroelectricity, and high chemical stability [45–47]. The structure comprises alternating $(Bi_2O_2)^{2+}$ fluorite-like layers and perovskite-like $(Bi_2Ti_3O_{10})^{2-}$ blocks, resulting in pronounced anisotropy and spontaneous polarization [48]. This built-in polarization field is highly effective in suppressing e^-–h^+ recombination and improving photocatalytic activity. As a result, BTO has been widely explored for applications in photocatalytic water splitting, pollutant degradation, and solar energy conversion [45,46,49–51]. Nonetheless, pristine BTO still suffers from moderate activity and limited surface and electronic properties, restricting its practical application.

To address these limitations, tailoring ferroelectric properties offers a promising alternative to conventional band gap engineering [46,49] or surface modification [43,52–54]. Among available strategies, chemical doping is particularly effective in tuning ferroelectric behavior and enhancing photocatalysis [32,42,55]. In this context, rare-earth element doping at the A-site of BTO improves structural symmetry, reduces oxygen vacancy concentrations, and stabilizes ferroelectric domains. La^{3+} doping is especially advantageous because its ionic radius closely matches that of Bi^{3+}, minimizing lattice distortion [56]. Furthermore, the incorporation of La^{3+} ions reduces local lattice distortion and enhances crystallinity and domain switching behavior, collectively leading to improved remanent polarization (P_r) [57,58]. These structural and ferroelectric enhancements directly improve charge separation and extend carrier lifetimes, both of which are essential for efficient photocatalysis. Among La-doped $Bi_{4-x}La_xTi_3O_{12}$ compositions, $Bi_{3.25}La_{0.75}Ti_3O_{12}$ (La-BTO) has been identified as an optimal formulation, exhibiting a well-balanced combination of polarization strength, structural stability, and photocatalytic activity [48,59,60]. Previous studies have demonstrated its superior polarization retention and robust piezophotocatalytic performance, yet the fundamental role of ferroelectric polarization in modulating charge carrier dynamics and driving photocatalytic reactions remains insufficiently explored. Moreover, it is crucial to differentiate the intrinsic effect of polarization from other influencing factors, such as band structure and surface area, to achieve a deeper mechanistic understanding.

In this study, ferroelectric polarization, identified as the principal factor governing the photocatalytic degradation of TC, was systematically investigated. By comparing pristine BTO, La-doped BTO, and depolarized BTO (D-BTO), which possess similar crystal structures and band gaps but differ in polarization states, the contribution of spontaneous polarization to charge separation and photocatalytic efficiency was elucidated. The results demonstrate that La doping enhances P_r, facilitates carrier separation, and markedly improves photocatalytic performance. Among the samples, La-doped BTO with the strongest polarization exhibited the highest photocurrent and the longest carrier lifetime, confirming the decisive role of the polarization electric field. Conversely, depolarization treatment significantly weakened charge separation and suppressed photocatalytic activity, providing compelling evidence that ferroelectric polarization is the dominant internal mechanism driving photocatalysis in BTO-based systems. Collectively, this work establishes a comprehensive framework for understanding the relationship between ferroelectric polarization and photocatalytic behavior. Furthermore, these findings provide a blueprint for developing next-generation, polarization-driven functional materials for energy conversion and environmental remediation, extending beyond BTO to a broader class of ferroelectric systems.

2 Experimental

2.1 Materials

$La(NO_3)\cdot 6H_2O$ (99.0%), $Ti(OC_4H_9)_4$ (99.0%), p-benzoquinone (p-BQ; 99.0%), and tetracycline ($C_{22}H_{24}N_2O_8$; 98.0%) were purchased from Shanghai Aladdin Bio-Chem Technology Co., Ltd. (China). $Bi(NO_3)_3\cdot 5H_2O$ (99.0%), NaOH, methanol (MeOH, 99.5%), and isopropanol (IPA; 99.7%) were obtained from Sinopharm Chemical Reagent Co., Ltd. (China). $AgNO_3$ (99.0%) was supplied by Guangdong Guanghua Sci-Tech Co., Ltd. (China).

2.2 Catalyst preparation

2.2.1 Preparation of BTO

3.2 mmol of $Bi(NO_3)_3\cdot 5H_2O$ was dissolved in 30 mL of 3 M NaOH under continuous stirring for 30 min. Subsequently, 2.4 mmol of $Ti(OC_4H_9)_4$ was added, and the mixture was stirred for an additional 30 min at room temperature. The resulting suspension was transferred into a 100 mL Teflon-lined autoclave and subjected to hydrothermal treatment at 180 °C for 18 h. After cooling to room temperature, the precipitate was collected by centrifugation, washed three times with deionized water and absolute ethanol, and finally dried at 80 °C for 8 h.

2.2.2 Preparation of La-doped BTO ($Bi_{4-x}La_xTi_3O_{12}$)

$0.8\times(4-x)$ mmol of $Bi(NO_3)_3\cdot 5H_2O$ (x = 0.3, 0.75, 1.0) was dissolved in 30 mL of 3 M NaOH and stirred for 30 min. 2.4 mmol of $Ti(OC_4H_9)_4$ was then added, followed by stirring for 30 min. Subsequently, $0.8x$ mmol of $La(NO_3)\cdot 6H_2O$ was introduced, and stirring continued until a homogeneous solution was obtained. The mixture was transferred to a 100 mL Teflon-lined autoclave and hydrothermally treated at 180 °C for 18 h. After cooling to room temperature, the precipitate was collected by centrifugation. The product was collected, washed, and dried using the same procedure described for BTO. The samples were named 0.3La-BTO (x = 0.3), 0.75La-BTO (x = 0.75), and 1.0La-BTO (x = 1.0).

2.2.3 *Preparation of depolarized BTO*

The as-prepared BTO powders were placed in a tube furnace, heated to 700 °C at a rate of 10 °C/min, and calcined at 700 °C for 1 h, followed by natural cooling to room temperature.

2.3 Characterization

X-ray diffraction (XRD) patterns were recorded on a Philips X' pert PRO diffractometer with Cu Kα radiation. Field emission scanning electron microscopy (FE-SEM) was performed on a Quantum 200FEG SEM, and transmission electron microscopy (TEM) was carried out on a Talos F200x G2 (FEI). An X-ray photoelectron spectrometer (XPS; K-Alpha, Thermo) was used to determine elemental valence states. Optical properties were characterized using a UV–Vis diffuse reflectance spectrometer (UV–Vis DRS; UV-2910, HITACHI). Time-resolved photoluminescence (TRPL) spectra were collected on an Edinburgh FLS1000 spectrometer. Piezoresponse force microscope/Kelvin probe force microscope (PFM/KPFM; Dimension Icon, Bruker) was employed to confirm domain structures and surface potentials. An electrochemical workstation (CHI660E, Chenhua) and a xenon lamp light source system (CEL-HXF300-S, Beijing China Education AuLight Technology Co., Ltd.) were used to assess the photoelectrochemical performance. An electron paramagnetic resonance spectrometer (EPR; EMXplus, Bruker) was used to identify reactive species. High-performance liquid chromatography–mass spectrometry (LC–MS) was used for qualitative analysis of TC degradation products. Ferroelectric and leakage current properties were evaluated using a Precision Premier II (Radiant Technologies).

2.4 Electrochemical measurements

Electrochemical measurements were conducted using a CHI760E electrochemical workstation (Chenhua) in a three-electrode configuration. A graphite electrode and a saturated calomel electrode (SCE) served as the counter and reference electrodes, respectively. The working electrode was prepared via drop-casting: 10 mg of catalyst was dispersed in 750 μL of deionized water, 250 μL of isopropanol, and 100 μL of Nafion solution, followed by ultrasonication for 30 min. A 100 μL aliquot of the suspension was drop-cast onto an indium tin oxide (ITO) substrate (1 cm × 2 cm) and dried at 80 °C for 8 h. All tests were performed in 0.5 M Na_2SO_4 electrolyte under illumination from the same light source used in the photocatalytic experiments.

2.5 Photocatalytic activity test

The photocatalytic activity of the catalyst was evaluated through the degradation of TC under light irradiation. Typically, 25 mg of catalyst was dispersed in 50 mL of TC solution (50 mg/L). Prior to irradiation, the suspension was magnetically stirred in the dark for 30 min to establish adsorption–desorption equilibrium. Photocatalytic reactions were carried out under a xenon lamp light source system. During irradiation, 2 mL aliquots were collected at 5-min intervals, filtered through a 0.22 μm syringe filter, and analyzed using a UV–Vis spectrophotometer (721G, INESA) at the characteristic absorption wavelength of 357 nm. The cycling stability was evaluated through five consecutive photocatalytic degradation cycles of TC at 50 mg/L under identical experimental conditions. After each cycle, the La-BTO photocatalyst was collected by centrifugation, thoroughly washed with deionized water and ethanol, and then dried at 60 °C before reuse.

3 Results and discussion

3.1 Structural and morphological characterization

The XRD patterns of pristine BTO, D-BTO, and La-BTO (Fig. 1(a)) confirm the successful formation of the Aurivillius phase without detectable secondary phases, indicating that La^{3+} doping and depolarization treatment do not alter the overall crystal structure. All samples exhibit diffraction peaks characteristic of the orthorhombic BTO phase (JCPDS#72-1019), demonstrating the structural compatibility of La incorporation. Neither La doping nor depolarization induced any obvious peak shift, further confirming that the crystalline phase of BTO remains unchanged. Notably, D-BTO exhibits sharper and more intense peaks, suggesting improved crystallinity as a result of high-temperature annealing.

SEM images (Figs. 1(b)–1(d)) reveal a consistent lamellar morphology across all samples, where stacked nanosheets assemble into hierarchical flower-like structures. This architecture provides a large surface area and multiple exposed active facets, both of which are advantageous for photocatalytic reactions. The layered crystal structure, characterized by low bonding energy in the *a*–*b* plane, facilitates lateral growth of nanosheets during hydrothermal synthesis, resulting in the observed morphology. Furthermore, the nanosheet-like configuration exposes a larger polar surface along the *a*–*b* plane and facilitates directional polarization, thereby enhancing the spatial separation of photogenerated charge carriers. The D-BTO sample exhibits a slightly thicker nanosheet structure, likely due to recrystallization and grain coarsening during annealing. Elemental mapping of La-BTO (Fig. S1 in the Electronic Supplementary Material (ESM)) clearly shows the presence of Bi, Ti, O, and La, indicating the successful incorporation of La into BTO. TEM further confirms the flower-like morphology and nanosheet stacking (Figs. 1(e) and 1(f)). The high-resolution TEM (HRTEM) image (Fig. 1(g)) shows lattice fringes with spacings of 0.270 and 0.271 nm, corresponding to the (020) and (200) planes, respectively [61].

XPS was conducted to investigate the chemical composition and oxidation states. The survey spectra (Fig. S2 in the ESM) reveal only Bi, Ti, and O signals for BTO and D-BTO, while La-BTO additionally shows La 3d peaks, confirming the successful incorporation of La, consistent with the XRD and SEM results. High-resolution XPS spectra of Bi 4f, Ti 2p, and O 1s are presented in Figs. 2(a)–2(c). The Bi 4f spectra (Fig. 2(a)) exhibit doublets centered at 164.1 and 158.8 eV, corresponding to Bi^{3+} species. Compared with pristine BTO, La-BTO shows a shift of Bi 4f peaks to lower binding energies, indicative of a more electron-rich environment caused by partial substitution of Bi^{3+} by La^{3+}. The smaller ionic radius and lower electronegativity of La^{3+} alter the local electronic environment, enhancing nuclear shielding and lowering the binding energy. The Ti 2p spectra (Fig. 2(b)) can be deconvoluted into peaks at 465.6, 463.3, and 457.6 eV, corresponding to Bi $4d_{3/2}$, Ti $2p_{1/2}$, and Ti $2p_{3/2}$, respectively. The energy separation of 5.7 eV between Ti $2p_{1/2}$ and Ti $2p_{3/2}$ confirms the Ti^{4+} oxidation state. D-BTO exhibits Ti 2p and Bi 4f peaks at nearly identical positions to those of pristine BTO, indicating unchanged chemical states after depolarization.

The O 1s spectra (Fig. 2(c)) can be deconvoluted into lattice oxygen (O_L, 529.3 eV) and oxygen vacancy-related oxygen (O_V, 530.9 eV) [62]. The proportion of O_V in La-BTO (11.5%) is lower than that in pristine BTO (14.3%), implying that La doping suppresses the formation of oxygen vacancy. The diminished oxygen vacancy concentration not only stabilizes the perovskite-like layered structure but also contributes to the electronic

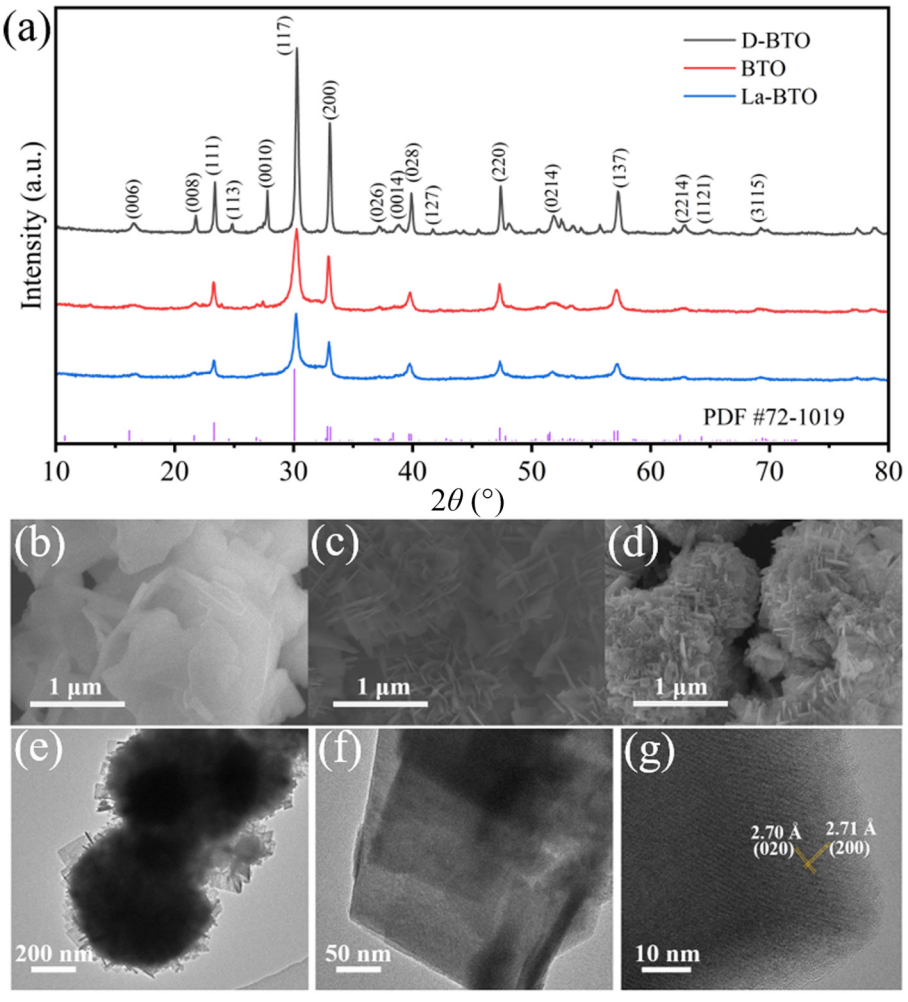

Fig. 1 (a) XRD patterns of D-BTO, BTO, and La-BTO; SEM images of (b) D-BTO, (c) BTO, and (d) La-BTO; (e, f) TEM image of La–BTO; (g) HRTEM image of La-BTO.

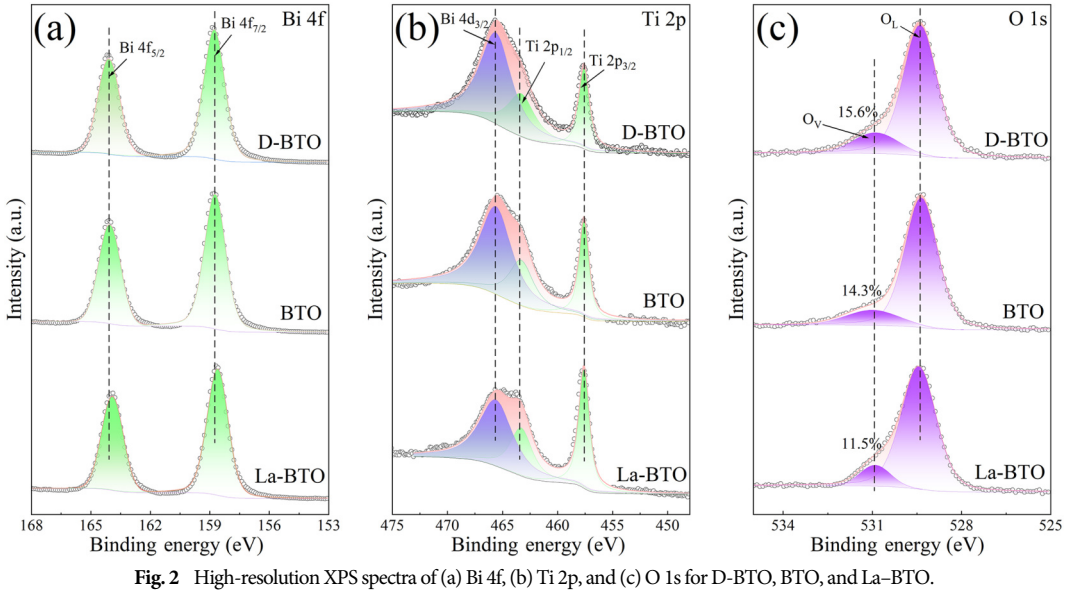

Fig. 2 High-resolution XPS spectra of (a) Bi 4f, (b) Ti 2p, and (c) O 1s for D-BTO, BTO, and La–BTO.

uniformity, further supporting the observed shift in Bi binding energy. Conversely, D-BTO exhibits a slightly higher O_V content (15.6%), which is attributed to the high-temperature depolarization process that facilitates the escape of lattice oxygen and the formation of O_V defects. This modest change in oxygen vacancies has a negligible impact on the structure and performance. Additionally, the La 3d spectra of La-BTO (Fig. S3 in the ESM) exhibit characteristic peaks at 855.6/852.0 eV (La $3d_{3/2}$) and 838.6/835.1 eV (La $3d_{5/2}$), confirming the existence of La^{3+}.

3.2 Optical properties and band structure

Generally, the optical absorption and band structure of catalysts are critical parameters that directly influence their light-harvesting efficiency and photocatalytic activity. UV–Vis DRS spectra (Fig. 3(a)) exhibit strong absorption across the UV–Vis region for all samples, with absorption edges at approximately 400 nm. The band gaps were estimated using Tauc plots derived from the Kubelka–Munk function (Fig. 3(b)) [63]. The values were 3.28 eV for BTO, 3.33 eV for La-BTO, and 3.17 eV for D-BTO, suggesting that La doping and depolarization exert minimal influence on the intrinsic band structure. Nonetheless, the slight shifts in the absorption edges may be associated with localized electronic states induced by La^{3+} substitution [64].

Mott–Schottky plots (Figs. 3(c)–3(e)) confirm that all samples are n-type semiconductors, as evidenced by their positive slopes. The flat band potentials (E_{fb}) were −1.19, −1.29, and −1.30 V (vs. SCE) for D-BTO, BTO, and La-BTO, respectively. For n-type semiconductors, the E_{fb} obtained from the Mott–Schottky plot is typically slightly more positive than the conduction band potential (E_{CB}) due to the presence of a surface depletion layer. The energy difference between E_{fb} and E_{CB} generally falls within the range of 0.1–0.3 V, depending on factors such as carrier concentration and surface states [65,66]. Converted to the normal hydrogen electrode (NHE) scale: $E_{fb,NHE} = E_{fb,SCE} + 0.244$ V [67,68], the E_{CB} was estimated by applying a 0.1 V correction: −1.05 V (D-BTO), −1.15 V (BTO), and −1.16 V (La-BTO). These values are more negative than the $O_2/\cdot O_2^-$ (−0.33 V) [23], indicating that photogenerated electrons can effectively reduce O_2. On the basis of the relationship between E_g and E_{CB}, the corresponding valence band positions (E_{VB}) were calculated to be 2.12 eV (D-BTO), 2.13 eV (BTO), and 2.17 eV (La-BTO), sufficiently positive to oxidize OH^- to ·OH radicals (1.99 V) [69]. Valence-band XPS (VB-XPS) spectra (Fig. S4 in the ESM) further support these results, showing similar energy differences between the valence band maximum (VBM) and Fermi level (1.56–1.61 eV), confirming nearly identical Fermi levels across the three samples. The band alignment diagrams (Fig. 3(f)) illustrate that all samples share comparable band structures, with minor differences in band gaps of 3.17–3.33 eV and minimal differences in band edge positions, indicating that the intrinsic electronic structure of BTO is largely preserved despite La doping or depolarization treatment.

These findings suggest that the enhanced photocatalytic activity observed in La-BTO (Section 3.3) is not primarily driven by energy band modulation. Instead, improvements are more

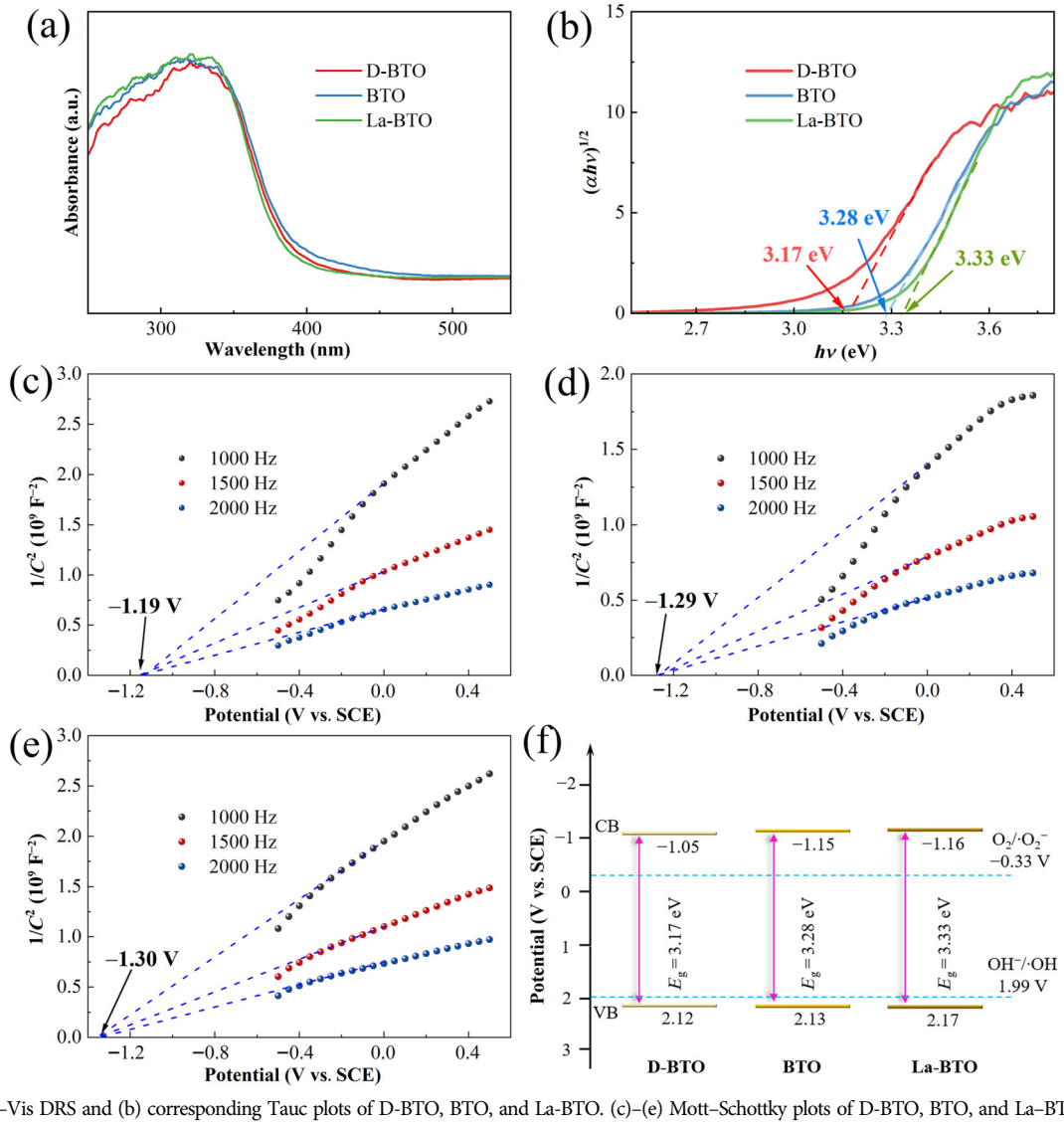

Fig. 3 (a) UV–Vis DRS and (b) corresponding Tauc plots of D-BTO, BTO, and La-BTO. (c)–(e) Mott–Schottky plots of D-BTO, BTO, and La–BTO, respectively. (f) Energy band diagram of D-BTO, BTO, and La-BTO.

清华大学出版社 Tsinghua University Press | SciOpen

attributed to polarization-induced effects, which facilitate charge separation and interfacial redox reactions. The nearly identical band gaps and energy levels across the samples highlight the role of ferroelectric polarization in governing carrier dynamics rather than light absorption capacity and band structure modulation.

3.3 Photocatalytic performance in TC degradation

The photocatalytic activity of the synthesized samples was evaluated by monitoring the degradation of TC under light irradiation. The optimal La doping concentration was determined through a series of photocatalytic experiments using $Bi_{4-x}La_xTi_3O_{12}$ samples with varying La contents (x = 0.0, 0.3, 0.75, and 1.0) (Fig. S5 in the ESM). As shown in Fig. 4(a), after 30 min of illumination, the degradation rates of D-BTO, BTO, and La-BTO were 40.7%, 70.7%, and 94.6%, respectively. These results clearly demonstrate a significant enhancement in photocatalytic activity, particularly with La doping. Control experiments conducted under light irradiation without a catalyst and under dark conditions with the catalyst (Fig. S6 in the ESM) confirmed that TC degradation primarily resulted from the photocatalytic process, with negligible contributions from self-degradation or piezocatalytic effects. To further assess the reaction kinetics, the degradation data were fitted using a pseudo-first-order kinetic model, as given by Eq. (1) [70]:

$$\ln(C_0/C_t) = kt \quad (1)$$

where C_0 and C_t are the initial and residual concentrations of TC, k is the reaction rate constant, and t is the reaction time. As shown in Fig. 4(b), the corresponding rate constants were determined to be 0.017 min^{-1} for D-BTO, 0.037 min^{-1} for BTO, and 0.087 min^{-1} for La-BTO. The degradation rate of La-BTO was approximately 5.1 times that of D-BTO and 2.4 times that of BTO, also surpassing most photocatalysts reported in the literature (Table S1 in the ESM).

As previously mentioned, D-BTO, BTO, and La-BTO exhibit similar band gaps and conduction/valence band positions; however, their photocatalytic efficiencies differ considerably. This discrepancy indicates that enhanced photocatalysis cannot be solely attributed to the band structure or light absorption. Furthermore, based on the results of the specific surface area measurements (Fig. S7 and Table S2 in the ESM), it can be inferred that surface area is not the dominant factor governing photocatalytic activity. Instead, ferroelectric polarization is believed to play a decisive role in determining the photocatalytic

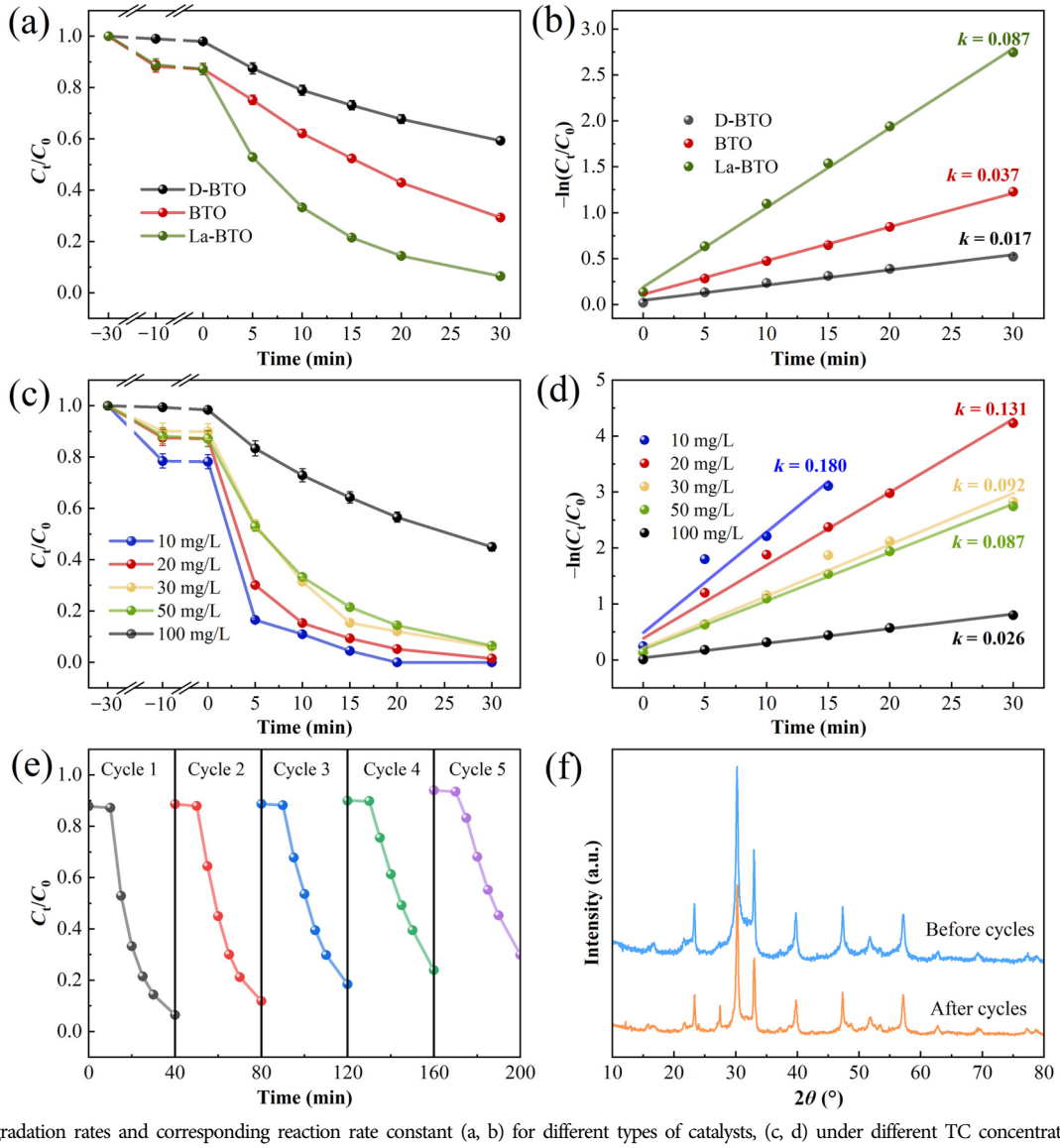

Fig. 4 TC degradation rates and corresponding reaction rate constant (a, b) for different types of catalysts, (c, d) under different TC concentrations. (e) Cyclic experiment of TC degradation. (f) XRD patterns of La-BTO before and after cycling.

efficiency. The superior activity of BTO compared with D-BTO highlights the contribution of polarization in facilitating charge carrier separation via internal electric fields. In D-BTO, thermal depolarization eliminates this field, accelerating e^-–h^+ recombination and limiting reactive species generation. In contrast, BTO retains spontaneous ferroelectric polarization, while La-BTO, with strengthened polarization, exhibits an even stronger internal electric field that further enhances charge separation and transfer. Thus, the pronounced improvement in La-BTO photocatalysis is attributed to polarization-driven carrier dynamics rather than intrinsic band structure modification. This hypothesis is further verified in subsequent analyses of carrier dynamics and polarization behavior.

Further investigation was conducted to evaluate the effect of the initial TC concentration on the photocatalytic performance of La-BTO. As shown in Fig. 4(c), when the TC concentration increased from 10 to 100 mg/L, the degradation rate within 30 min declined from 100%, 98.5%, 95.0%, and 94.6% to 55.0%. The corresponding pseudo-first-order rate constants (Fig. 4(d)) also decreased progressively, from 0.180 to 0.026 min^{-1} for concentrations of 10, 20, 30, 50, and 100 mg/L. The decrease in both the degradation rate and reaction rate constant with increasing TC concentration can be attributed to two factors. First, there is the inner filter effect, where higher TC concentrations absorb more incident photons and hinder light penetration to the photocatalyst surface. Second, the insufficient generation of reactive species to degrade the excess TC molecules leads to site saturation and reduced efficiency.

To assess the reusability and stability of the photocatalyst, cyclic degradation tests were conducted using La-BTO at a TC concentration of 50 mg/L over five successive runs. As depicted in Fig. 4(e), the degradation rate decreased from 94.6% in the first cycle to 70.0% in the fifth cycle, indicating moderate deactivation. Post-reaction XRD patterns (Fig. 4(f)) confirmed that the crystal structure remained unchanged, while SEM images (Fig. S8 in the ESM) showed a stable morphology. Furthermore, PFM was employed to examine its ferroelectric switching behavior before and after photocatalytic cycling. As presented in Fig. S9 in the ESM, the butterfly-like amplitude loops and 180° phase switching loops exhibited minor changes after five cycles, indicating that the intrinsic ferroelectric polarization was well retained and that the polarization switching behavior remained stable. Therefore, the performance decline is mainly attributed to surface fouling by degradation intermediates or partial deactivation of surface-active sites, rather than structural and polarization instability [71].

To further evaluate the universality and practical applicability of the photocatalyst, additional photocatalytic experiments were carried out in real water matrices and with other representative organic pollutants. As shown in Fig. S10 in the ESM, the La-BTO catalyst was evaluated using secondary effluent from a municipal wastewater treatment plant spiked with TC (50 mg/L). The La-BTO photocatalyst retained over 86% of its degradation efficiency compared with that in deionized water, demonstrating excellent adaptability and robustness in complex aqueous environments. Moreover, as shown in Fig. S11 in the ESM, the ferroelectric photocatalyst La-BTO also exhibited remarkable photocatalytic activity toward rhodamine B (RhB) and methylene blue (MB), confirming its broad-spectrum degradation capability. Specifically, 93.2% of RhB was degraded after 45 min of light irradiation, whereas 81.0% of MB was degraded after 60 min, further validating the wide applicability of the polarization-enhanced photocatalytic mechanism.

3.4 Carrier dynamics and ferroelectric polarization effects

The efficiency of photogenerated charge carrier separation and transfer is a critical factor determining the photocatalytic activity of semiconductors. To obtain comprehensive insights into these processes, a combination of photoelectrochemical and spectroscopic techniques was employed, including photocurrent-time measurements (*I*–*t*), open-circuit potential (OCP), electrochemical impedance spectroscopy (EIS), and TRPL.

The *I*–*t* responses (Fig. 5(a)) reveal that La-BTO exhibits the highest transient photocurrent (~0.50 μA/cm²) under intermittent illumination, which is substantially greater than that of pristine BTO (~0.11 μA/cm²) and D-BTO (~0.04 μA/cm²). This result suggests that La doping significantly improves the separation and transport of photogenerated carriers. As shown in Fig. 5(b), illumination decreases the potential of the photocatalyst electrode due to radical accumulation. The open-circuit photovoltage (V_{OC}) response further supports this finding, showing a markedly higher potential of −103.1 mV (vs. SCE) for La-BTO than that for BTO (−27.3 mV) and for D-BTO (−9.9 mV). The enhanced V_{OC} indicates the presence of a stronger built-in electric field in La-BTO, which effectively drives charge separation [72]. EIS Nyquist plots (Fig. 5(c)) provide additional evidence that La doping promotes efficient carrier separation and migration. The semicircle radius reflects the interfacial charge-transfer resistance, with smaller radii corresponding to faster electron transfer [45]. Among the three samples, La-BTO shows the smallest semicircle, indicating the lowest charge-transfer resistance, while D-BTO exhibits the largest semicircle, consistent with its suppressed polarization and poor carrier mobility. Under illumination, all samples display reduced arc radii (Fig. S12 in the ESM), attributed to increased carrier density and enhanced conductivity. Notably, La-BTO shows the lowest impedance under light excitation, consistent with its superior photocatalytic performance and confirming the role of ferroelectric polarization in facilitating carrier separation and transfer.

Carrier recombination dynamics were further investigated by TRPL spectroscopy (Figs. 5(d)–5(f)). The decay curves fit well to a multiexponential function, and the average PL lifetimes were calculated to be 26.82 ns (D-BTO), 12.90 ns (BTO), and 4.72 ns (La-BTO) (Table S3 in the ESM). For D-BTO, all three lifetime components (τ_1, τ_2, and τ_3) as well as the average lifetime exhibited an increase compared with pristine BTO. This prolongation of the PL lifetime can be attributed to the suppression of the ferroelectric polarization, which weakens the internal electric field and thus reduces the driving force for charge separation. As a result, photogenerated carriers are more likely to remain in the bulk and undergo radiative recombination, leading to an apparently longer PL decay. In contrast, La-BTO shows significantly shorter lifetimes. This reduction in carrier lifetime is not due to enhanced recombination but rather reflects the more efficient extraction of carriers driven by the strengthened ferroelectric polarization. The accelerated separation and interfacial transfer of carriers reduce the probability of bulk radiative recombination, thereby resulting in faster PL decay but ultimately promoting higher photocatalytic activity.

The superior carrier dynamics observed in La-BTO suggest the presence of an internal driving force associated with ferroelectric polarization. To verify this, the ferroelectric properties were examined. As shown in Figs. 6(a)–6(c), the PFM phase and amplitude images of D-BTO exhibited no distinct contrast or domain features. This lack of phase inversion and uniform amplitude response suggests that the ferroelectric domains were effectively eliminated after high-temperature depolarization. The

high-temperature annealing process effectively erased the long-range ferroelectric order, resulting in a nonferroelectric state with no observable domain structures. In contrast, both BTO and La–BTO display well-saturated rectangular ferroelectric hysteresis (*P*–*E*) loops at 20 kHz and at room temperature (Fig. 6(d)), indicating robust ferroelectric behavior. The P_r values are 19.3 μC/cm² for BTO and 26.1 μC/cm² for La-BTO, while the coercive fields ($2E_c$) are 418.2 and 387.6 kV/cm, respectively (Table S4 in the ESM). La doping slightly enhances P_r and reduces E_c, suggesting improved ferroelectric domain switchability and stability, which could facilitate polarization-driven charge separation. Leakage current characteristics (Fig. 6(e)) are comparable between BTO and La-BTO, with the latter exhibiting slightly reduced leakage due to fewer oxygen vacancies [73].

KPFM measurements (Fig. 7) further clarify the effect of polarization on surface potential. For D-BTO, the surface potential was nearly identical to that of the underlying ITO substrate, and no significant variation was observed upon light

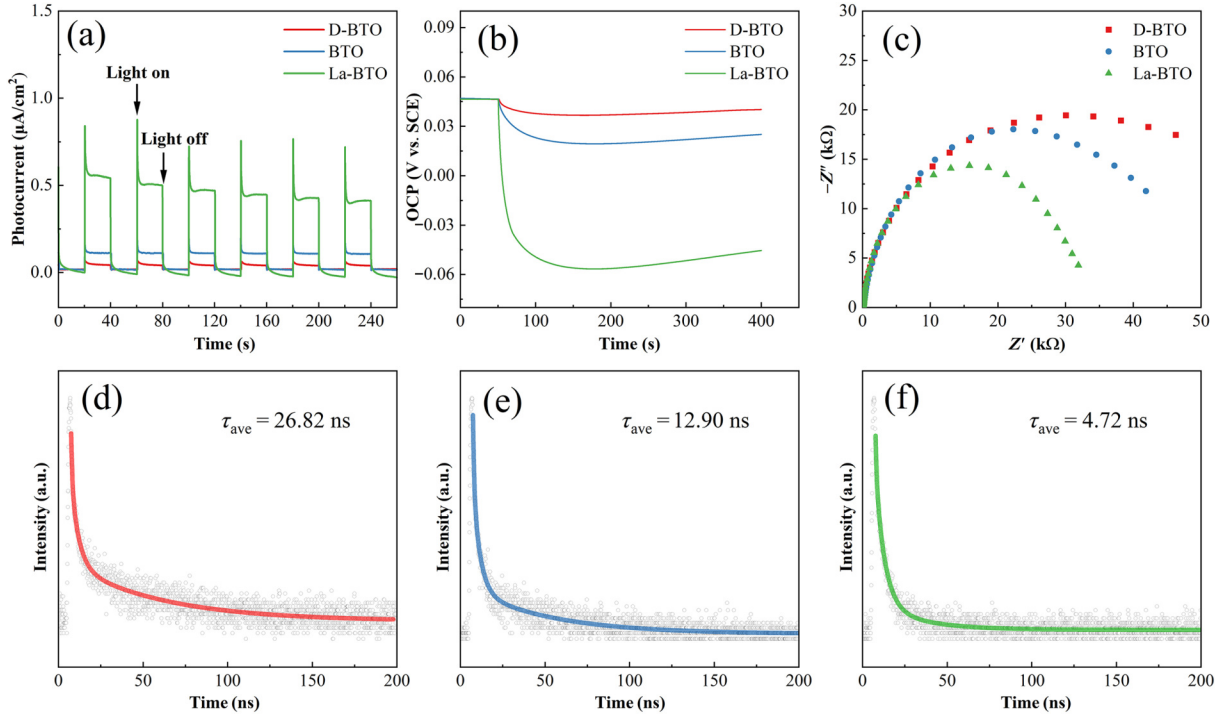

Fig. 5 (a) Transient photocurrent, (b) OCP, and (c) EIS Nyquist plots of D-BTO, BTO, and La-BTO. (d)–(f) TRPL spectra of D-BTO, BTO, and La-BTO, respectively.

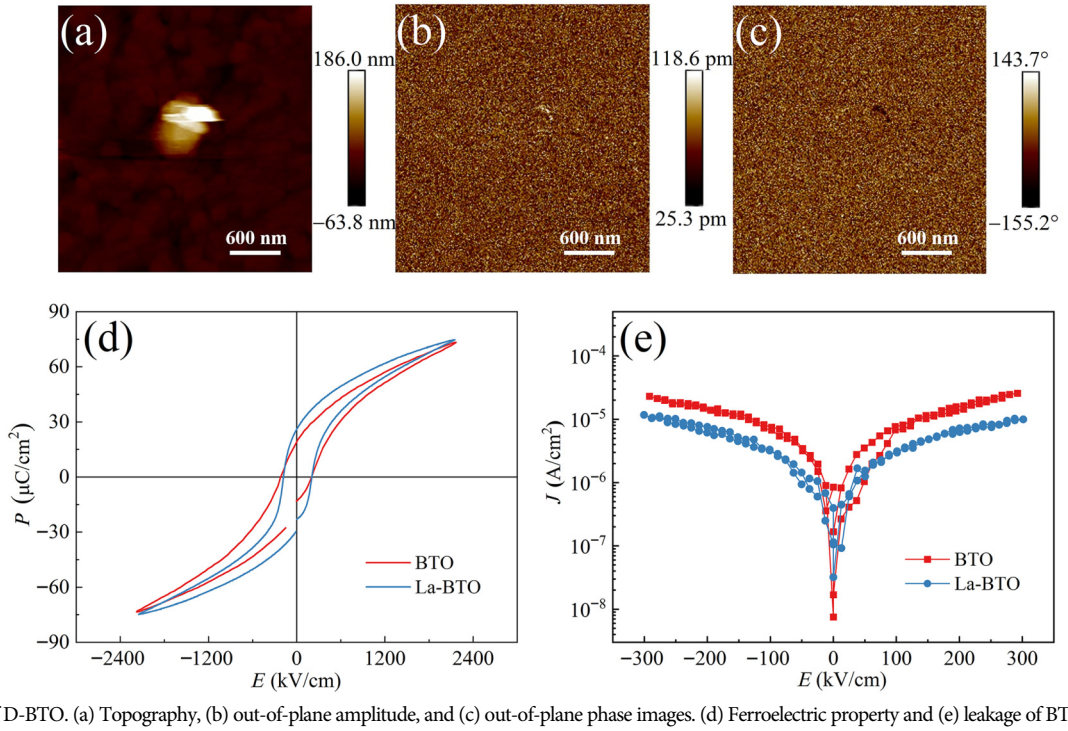

Fig. 6 PFM of D-BTO. (a) Topography, (b) out-of-plane amplitude, and (c) out-of-plane phase images. (d) Ferroelectric property and (e) leakage of BTO and La-BTO. Note that the ferroelectric data were obtained from the corresponding thin film samples.

illumination, as shown in Figs. 7(a)–7(c). This behavior indicates the absence of spontaneous polarization and internal electric fields, which can limit the generation and separation of photoinduced charge carriers at the surface. In contrast, BTO exhibits a higher surface potential than the ITO substrate in the dark, which decreased noticeably upon illumination (Figs. 7(d)–7(f)). The decrease in surface potential upon illumination arises from the accumulation of photogenerated electrons at the surface, which enhances charge screening and weakens the polarization-induced internal field, thus reducing the surface potential [49,74]. Such behavior is consistent with the moderate ferroelectric polarization of BTO and the presence of oxygen vacancies that act as compensating centers, partially neutralizing the polarization charges [75]. Notably, La-BTO exhibited the opposite trend, with the surface potential increasing under illumination (Figs. 7(g)–7(i)). This positive shift reveals that La doping suppresses oxygen vacancy formation, thereby reducing charge screening and stabilizing ferroelectric polarization. The strengthened and unscreened internal field in La-BTO directs photogenerated electrons along the polarization direction toward the bulk, while holes migrate toward the surface. This directional separation leads to an increase in surface potential under illumination. This positive shift confirms that the polarization field predominates over the screening effect, evidencing stronger and more stable ferroelectric polarization in La-BTO.

Collectively, these results highlight the decisive role of ferroelectric polarization in enhancing photocatalytic performance. The internal electric field induced by polarization promotes spatial separation of e^-–h^+ pairs, suppresses recombination losses, and accelerates interfacial redox processes, thereby improving the degradation rate of TC. Importantly, while La doping strengthens ferroelectric polarization, it has a negligible impact on the intrinsic band structure, as the band edges are primarily determined by the electronic orbitals of Bi, Ti, and O. Instead, La-induced lattice distortion enhances dipole alignment and polarization strength, thereby increasing the internal field without altering band positions. Thus, ferroelectric polarization acts as a carrier-modulation mechanism rather than a band-engineering strategy, providing an effective means to improve photocatalytic activity by facilitating charge separation and transfer.

3.5 Radical species and mechanistic verification

To identify the primary reactive species involved in the photocatalytic degradation of TC, EPR spectroscopy was conducted on La-BTO under light irradiation. As shown in Fig. 8, distinct signals corresponding to superoxide radicals ($\cdot O_2^-$, Fig. 8(a)) and hydroxyl radicals (·OH, Fig. 8(b)) were observed, while no evident signals of photogenerated holes or singlet oxygen ($^1O_2$) were detected (Fig. S13 in the ESM). The intensity of $\cdot O_2^-$

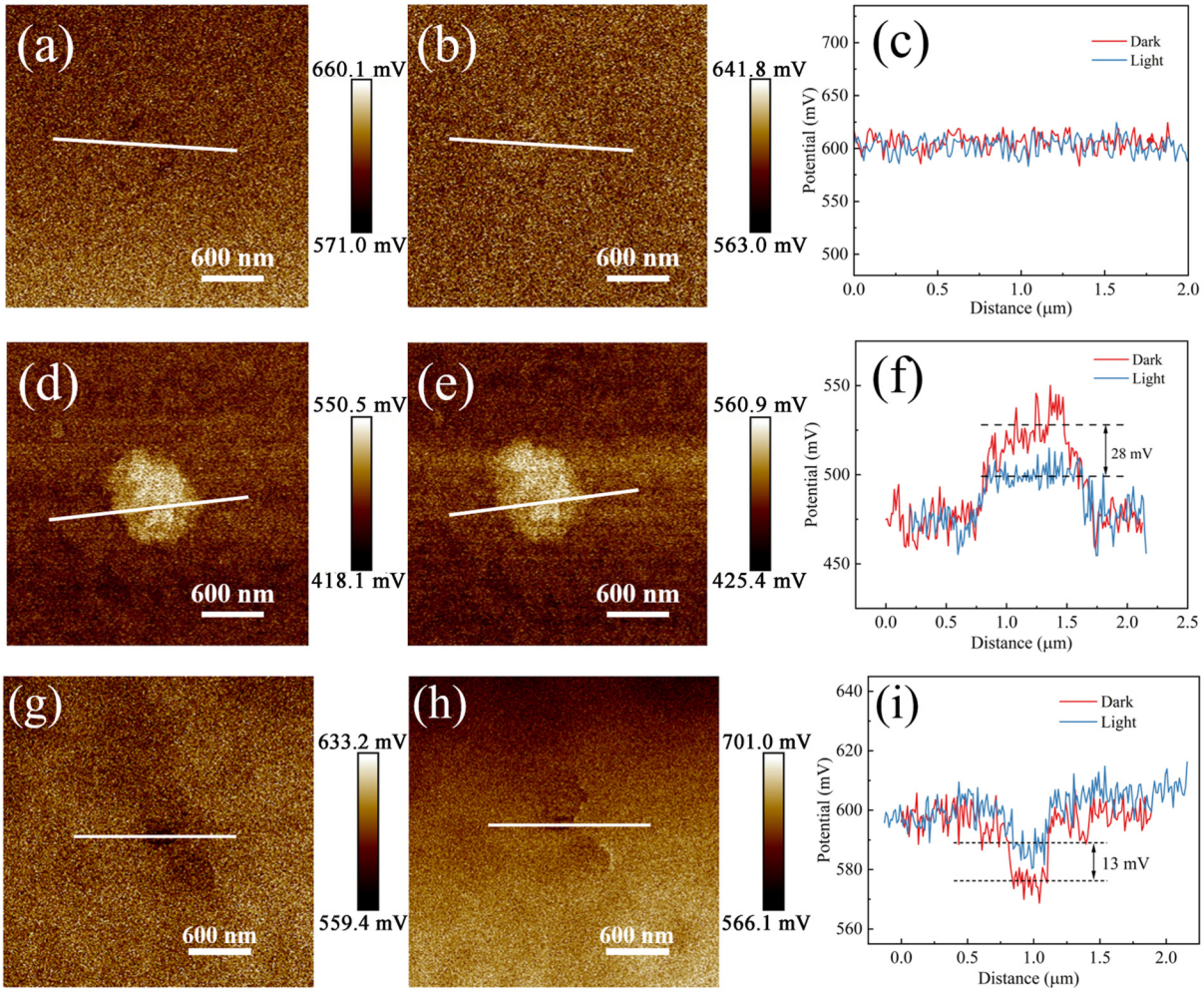

Fig. 7 KPFM studies of D-BTO, BTO, and La-BTO. Surface potential images of D-BTO (a) in dark and (b) light, (c) corresponding surface potential curves along white lines in (a, b). Surface potential images of BTO (d) in dark and (e) light, (f) corresponding surface potential curves along white lines in (c, d). Surface potential images of La-BTO in (g) dark and (h) light, and (i) corresponding surface potential curves along white lines in (g, h).

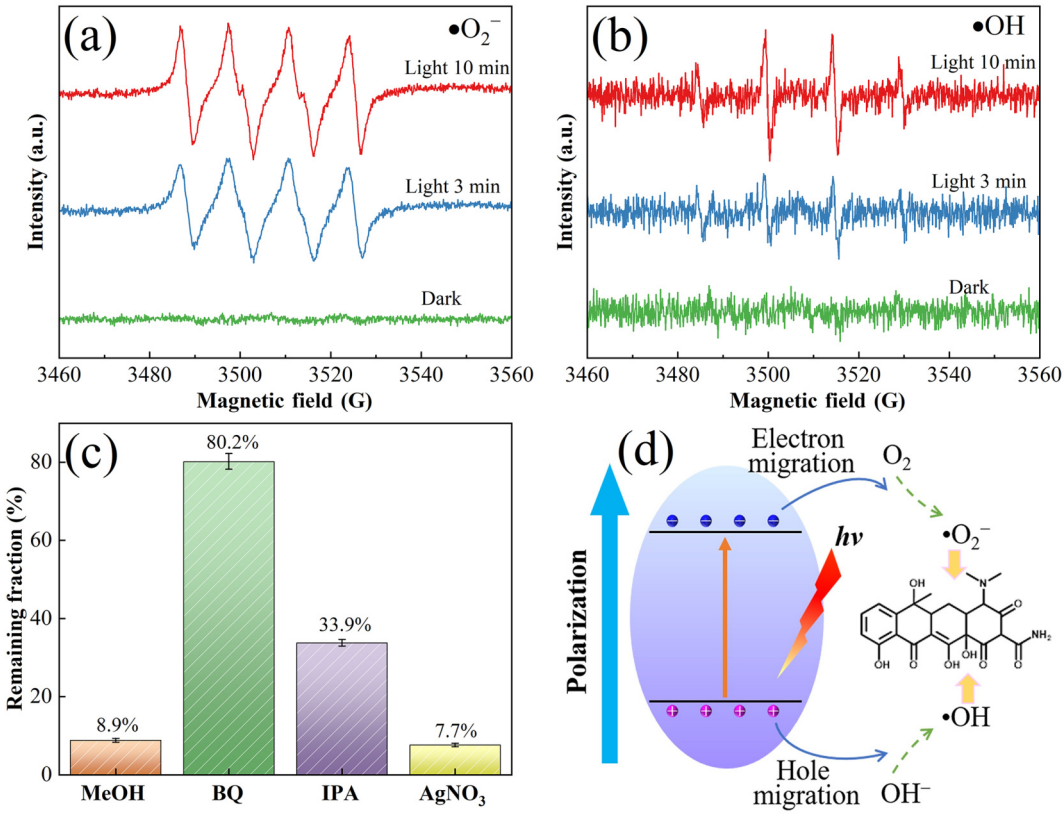

Fig. 8 EPR spectra of (a) 5,5-dimethyl-1-pyrroline N-oxide (DMPO)–·O_2^- and (b) DMPO–·OH. (c) Effects of various reactive species quenchers on TC degradation. (d) Proposed mechanism for photocatalytic degradation of TC by ferroelectric La-BTO.

and ·OH signals increased with prolonged illumination, indicating continuous generation of these species during photocatalysis. The strong ·O_2^- signal suggests that photogenerated e^- efficiently reduces surface-adsorbed O_2 molecules, which play a dominant role in TC degradation. The absence of detectable h^+ signals does not imply their absence but rather reflects their short lifetimes or rapid trapping. Notably, these EPR results are consistent with the band structure of La-BTO (Fig. 3(f)). Since the E_{CB} of La-BTO is more negative than the reduction potential of ·O_2/·O_2^- (−0.33 eV), photogenerated electrons can readily reduce O_2 to ·O_2^-. Similarly, the E_{VB} of La-BTO is more positive than the oxidation potential of OH^-/·OH (1.99 eV) [19], allowing the generation of ·OH radicals. Together, these observations confirm the formation of both ·O_2^- and ·OH radicals during photocatalysis.

To further clarify their roles, scavenger experiments were conducted, as illustrated in Fig. 8(c). $AgNO_3$, MeOH, IPA, and p-BQ were used as scavengers for electrons, holes, ·OH, and ·O_2^-, respectively. The addition of p-BQ resulted in a drastic suppression of photocatalytic activity, confirming ·O_2^- as the dominant reactive species. IPA also reduced the degradation rate, although to a lesser extent, demonstrating the secondary contribution of ·OH radicals. In contrast, MeOH and $AgNO_3$ had negligible effects, further confirming that direct hole oxidation or electron reduction are not major pathways under these conditions. Collectively, these results establish that TC degradation in La-BTO is primarily driven by ·O_2^- radicals, with ·OH radicals playing a supplementary role.

A schematic illustration of the proposed photocatalytic mechanism is presented in Fig. 8(d). Upon light excitation, La-BTO generates e^-–h^+ pairs. The enhanced ferroelectric polarization produces a stronger internal electric field across the nanosheets, which promotes directional migration of carriers to the surface and suppresses bulk recombination. Surface-trapped photoinduced electrons reduce O_2 to ·O_2^-, while holes oxidize OH^-/H_2O to produce ·OH. These reactive oxygen species synergistically decompose TC molecules into smaller, less toxic products. The overall process can be described by Reactions (2)–(6) [18,76]:

$$\text{Catalyst} + h\nu \rightarrow e^- + h^+ \quad (2)$$

$$O_2 + e^- \rightarrow \cdot O_2^- \quad (3)$$

$$H_2O \leftrightarrow H^+ + OH^- \quad (4)$$

$$h^+ + OH^- \rightarrow \cdot OH \quad (5)$$

$$\cdot O_2^-/\cdot OH + TC \rightarrow \text{Decomposed products} \quad (6)$$

The photocatalytic behaviors of D-BTO, BTO, and La-BTO, which exhibit systematically varied polarization states, have been compared to elucidate the role of ferroelectric polarization in the photocatalytic degradation of TC. Notably, despite their comparable band structures, the three samples showed markedly different photocatalytic activities, with La-BTO achieving the highest degradation rate and D-BTO the lowest. This trend highlights the central role of polarization rather than band structure in modulating photocatalytic performance. The internal electric field arising from spontaneous polarization in ferroelectric materials plays a crucial role in enhancing charge carrier dynamics. In BTO, spontaneous polarization facilitates electron–hole separation, while La substitution enhances this polarization, thereby strengthening the internal electric field. This effect is corroborated by the higher photocurrent density, larger

photovoltage, lower charge-transfer resistance, and shorter PL lifetime observed for La-BTO. In contrast, the depolarization treatment (D-BTO) suppressed ferroelectricity, resulting in poor charge separation, severe recombination, and inferior photocatalytic activity.

These results demonstrate that La doping does not significantly alter the intrinsic band structure of BTO. Instead, the improvement in photocatalytic performance arises from polarization-induced modulation of carrier dynamics. By enhancing charge separation and migration, ferroelectric polarization promotes the formation of reactive oxygen species, particularly $\cdot O_2^-$, which drive the efficient photocatalytic degradation of TC.

3.6 Degradation pathway and toxicity evaluation

To elucidate the degradation process of TC and assess the safety of its byproducts, the transformation pathways and toxicity of TC were systematically investigated. The degradation products generated under light irradiation with La-BTO as the photocatalyst were analyzed using LC–MS. LC–MS analyses of the reaction solution at 10 and 30 min were performed to identify intermediates and byproducts, with the corresponding mass spectra shown in Figs. S14(a) and S14(b) in the ESM. After 10 min of irradiation, nine major intermediates with mass-to-charge (m/z) values of 475, 453, 445, 413, 393, 349, 306, 301, and 223 were detected, along with smaller fragments (m/z = 164, 149, 74, 60). After 30 min, the dominant intermediates were reduced to six larger species (m/z = 393, 349, 306, 301, 223, and 164), accompanied by smaller fragments (m/z = 159, 74, and 60). As shown in Fig. S8 in the ESM, longer irradiation resulted in a higher proportion of low-molecular-weight products, indicating progressive mineralization. The proposed structures, formulas, and m/z values of the detected intermediates are summarized in Table S5 in the ESM, and the inferred degradation pathway is illustrated in Fig. 9(a). The LC–MS results suggest that TC (m/z = 445) undergoes stepwise degradation through decarboxylation, hydroxylation, ring cleavage, and oxidative dehydrogenation. Specifically: In pathway I, under the attack of $\cdot O_2^-$ and ·OH radicals, the N–CH_3 group of TC is oxidized to the N–CHO group in product T_1 (m/z = 475) [77,78], followed by deamination and ring opening via ·OH attack, producing T_2 (m/z = 453) [79]. In pathway II, TC is attacked by $\cdot O_2^-$ and ·OH to generate T_3 (m/z = 393), which subsequently undergoes ring opening to form T_5 (m/z = 349) [79]. In pathways III and IV, TC undergoes oxidation, demethylation, and deamidation under the action of $\cdot O_2^-$ and ·OH, producing intermediates T_4 (m/z = 413) and T_8 (m/z = 306), which further transform by ring opening, dehydration, and deamination into T_6 (m/z = 301) and T_9 (m/z = 164) [80]. T_6 is subsequently cleaved by ·OH to generate T_7 (m/z = 223) [81]. These unstable intermediates are further oxidized into low-molecular-weight compounds such as T_{10} (m/z = 159), T_{11} (m/z = 149), T_{12} (m/z = 74), and T_{13} (m/z = 60) [80] and are ultimately mineralized into inorganic end-products, including H_2O, CO_2, and NH_4^+ [82–84].

The toxicity of TC and its intermediates was predicted using the Toxicity Estimation Software Tool (T.E.S.T.), with fathead minnow LC_{50} (96 h), developmental toxicity, and mutagenicity as evaluation parameters [85,86]. As depicted in Fig. 9(b), the LC_{50} values revealed that most intermediates were less toxic than TC, with T_3, T_{11}, T_{12}, and T_{13} exhibiting markedly higher LC_{50} values, indicating lower toxicity. Developmental toxicity simulations (Fig. 9(c)) showed that TC itself was toxic (value = 0.86), whereas most intermediates exhibited reduced developmental toxicity relative to TC. Mutagenicity assessments (Fig. 9(d)) further demonstrated that the majority of intermediates were less mutagenic than TC. A mutagenicity index below 0.5 indicates negative results, and all intermediates except T_1, T_3, T_4, and T_5 fell into this category. Importantly, progressive degradation leads to

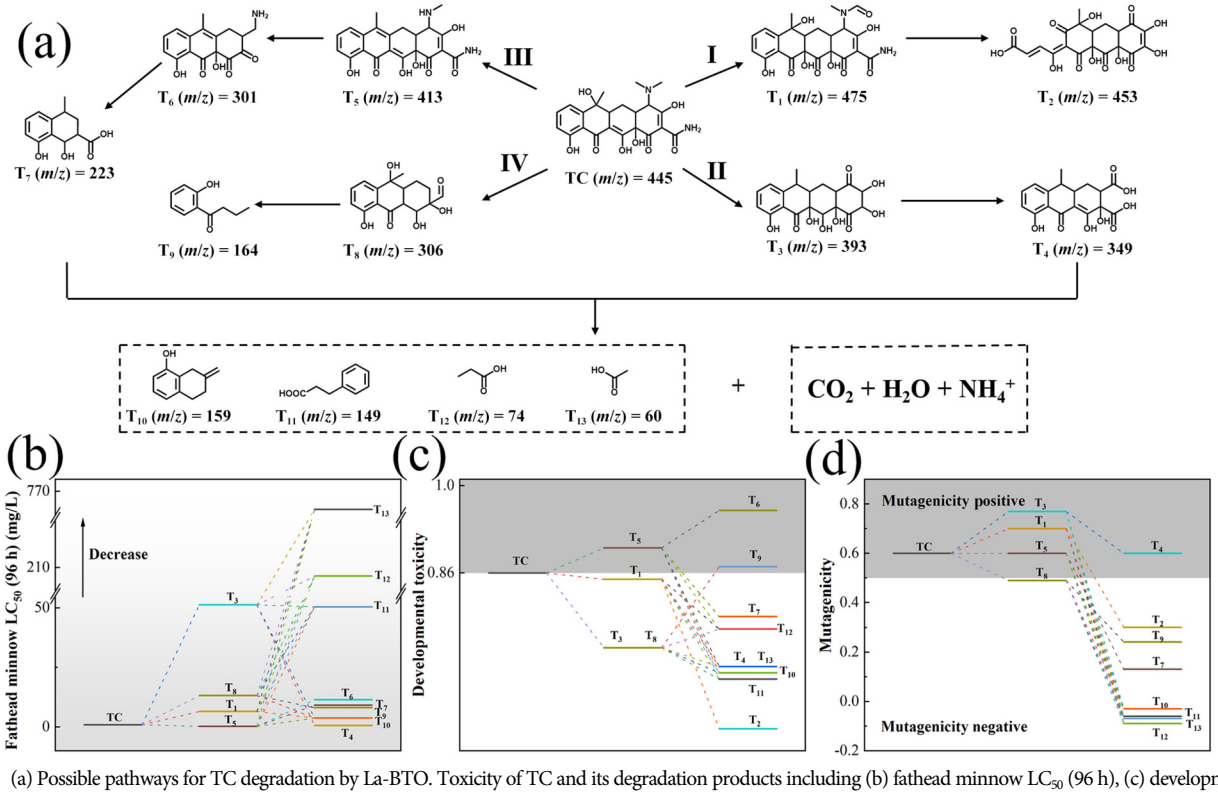

Fig. 9 (a) Possible pathways for TC degradation by La-BTO. Toxicity of TC and its degradation products including (b) fathead minnow LC_{50} (96 h), (c) developmental toxicity, and (d) mutagenicity.

extensive mineralization into nontoxic small molecules such as CO_2 and H_2O, further reducing ecological risk. Taken together, these results demonstrate that photocatalytic degradation of TC by La-BTO proceeds through multistep oxidation, ring opening, and deamination pathways, yielding progressively smaller and less toxic intermediates. The transformation not only enhances mineralization but also substantially reduces overall toxicity, thereby confirming the potential of La-BTO photocatalysis for mitigating the environmental hazards of TC.

4 Conclusions

In summary, BTO and La-BTO photocatalysts were synthesized via a hydrothermal method, while D-BTO was prepared as a control to decouple the effect of ferroelectric polarization. Despite exhibiting comparable band structures, the three samples showed markedly different photocatalytic activities toward TC degradation: La-BTO achieved a degradation rate of 94.6% within 30 min at an initial concentration of 50 mg/L, which was significantly higher than that of pristine BTO (70.7%) and D-BTO (40.7%). The superior performance of La-BTO is attributed to the enhanced ferroelectric polarization induced by La substitution, which facilitates directional charge migration and suppresses bulk recombination under visible-light irradiation. This polarization-driven charge separation mechanism was corroborated by EIS, photocurrent responses, and TRPL, all evidencing more efficient charge transport in La-BTO. Consequently, La-BTO exhibited the highest photocatalytic efficiency toward TC degradation, primarily through the generation of $\cdot O_2^-$ and ·OH radicals. Beyond improving photocatalytic activity, these findings advance the understanding of how ferroelectric polarization modulates interfacial redox processes. This work demonstrates the critical role of polarization engineering in photocatalysis and highlights a rational strategy for designing high-performance ferroelectric photocatalysts for environmental remediation.

Acknowledgements

The research was financially supported by the Youth Funding of Hunan Provincial Education Department (No. 23B0443), the State Key Laboratory of New Ceramic Materials Tsinghua University (No. KFZD202403), the Anhui Provincial Natural Science Foundation (No. 2408085ME116), and the National Natural Science Foundation of China (Nos. 12474095 and 52402323).

Author contributions

Yi Xu: formal analysis and investigation, methodology, conceptualization. Guoping Wang: resources, investigation. Bingbing Yang: writing - review and editing, funding acquisition. Yitong Li: investigation. Le Chen: formal analysis. Ruibin Wang: resources. Hongqing Wang: resources, supervision. Linghua Jin: writing - original draft preparation, funding acquisition, conceptualization, visualization.

Availability of data and materials

The data that support the findings of this study are available from the corresponding author upon reasonable request.

Competing interests

The authors have no competing interests to declare that are relevant to the content of this article.

Electronic Supplementary Material

Supplementary material is available in the online version of this article at https://doi.org/10.26599/JAC.2026.9221248.

References

[1] Patel M, Kumar R, Kishor K, *et al.* Pharmaceuticals of emerging concern in aquatic systems: Chemistry, occurrence, effects, and removal methods. *Chem Rev* 2019, **119**: 3510–3673.

[2] Hussain A, Ashique S, Zaheen Hassan M, *et al.* Pharmaceutical contaminants in aquatic systems, conventional and green strategies, recent updates, challenges and policies, and potential outcomes. *J Mol Liq* 2023, **389**: 122905.

[3] Sonkar V, Venu V, Nishil B, *et al.* Review on antibiotic pollution dynamics: Insights to occurrence, environmental behaviour, ecotoxicity, and management strategies. *Environ Sci Pollut R* 2024, **31**: 51164–51196.

[4] Thangrongthong S, Ladda B, Sittisom P. A review of antibiotic contamination in wastewater: Sources, impacts, and microbial bioremediation techniques. *Water Environ Res* 2025, **97**: 70118.

[5] Gao JW, Bai CY, Zheng T, *et al. In-situ* growth of MOFs on porous geopolymer spheres for continuous-flow PMS degradation of antibiotics. *J Adv Ceram* 2025, **14**: 9221114.

[6] Kim DY, McElvania E. Review of novel third-generation tetracyclines: Eravacycline, omadacycline, and sarecycline. *Clin Microbiol Newsl* 2023, **45**: 61–67.

[7] Pearson JC, Gillett E, Gadri ND, *et al.* Tetracyclines, the old and the new: A narrative review. *CMI Commun* 2025, **2**: 105059.

[8] Ghoreishian SM, Raju GSR, Pavitra E, *et al.* Ultrasound-assisted heterogeneous degradation of tetracycline over flower-like rGO/$CdWO_4$ hierarchical structures as robust solar-light-responsive photocatalysts: Optimization, kinetics, and mechanism. *Appl Surf Sci* 2019, **489**: 110–122.

[9] Daghrir R, Drogui P. Tetracycline antibiotics in the environment: A review. *Environ Chem Lett* 2013, **11**: 209–227.

[10] Li Q, Zheng YH, Guo LJ, *et al.* Microbial degradation of tetracycline antibiotics: Mechanisms and environmental implications. *J Agr Food Chem* 2024, **72**: 13523–13536.

[11] Ghoreishian SM, Raju GSR, Ranjith KS, *et al.* Construction of 2D/2D /2D rGO/p-C_3N_4/$Cu_3Mo_2O_9$ heterostructure as an efficient catalytic platform for cascade photo-degradation and photoelectrochemical activity. *Appl Surf Sci* 2020, **511**: 145469.

[12] Leichtweis J, Vieira Y, Welter N, *et al.* A review of the occurrence, disposal, determination, toxicity and remediation technologies of the tetracycline antibiotic. *Process Saf Environ* 2022, **160**: 25–40.

[13] Ahmad Aghapour A, Alizadeh N, Khorsandi H. Biological degradation and mineralization of tetracycline antibiotic using SBR equipped with a vertical axially rotating biological bed (SBR-VARB). *Biodegradation* 2023, **34**: 325–340.

[14] Gopal G, Alex SA, Chandrasekaran N, *et al.* A review on tetracycline removal from aqueous systems by advanced treatment techniques. *RSC Adv* 2020, **10**: 27081–27095.

[15] Chen XL, Yang YY, Ke YC, *et al.* A comprehensive review on biodegradation of tetracyclines: Current research progress and prospect. *Sci Total Environ* 2022, **814**: 152852.

[16] He XH, Kai TH, Ding P. Heterojunction photocatalysts for degradation of the tetracycline antibiotic: A review. *Environ Chem Lett* 2021, **19**: 4563–4601.

[17] Saadati F, Keramati N, Ghazi MM. Influence of parameters on the photocatalytic degradation of tetracycline in wastewater: A review. *Crit Rev Env Sci Tec* 2016, **46**: 757–782.

[18] Sun JL, Wu HZ, Fu CH, *et al.* Novel Fenton-like system based on bifunctional MgO/g-C_3N_4 S-scheme heterojunction photoanode for efficient tetracycline degradation. *Appl Catal B—Environ* 2024, **351**: 123976.

[19] Gao KX, Hou L, An XQ, *et al.* BiOBr/MXene/gC_3N_4 Z-scheme heterostructure photocatalysts mediated by oxygen vacancies and MXene quantum dots for tetracycline degradation: Process, mechanism and toxicity analysis. *Appl Catal B—Environ* 2023, **323**: 122150.

[20] Shi HF, Zhu HW, Jin T, *et al.* Construction of Bi/Polyoxometalate

doped TiO_2 composite with efficient visible-light photocatalytic performance: Mechanism insight, degradation pathway and toxicity evaluation. *Appl Surf Sci* 2023, **615**: 156310.
[21] Balakrishnan A, Kunnel ES, Sasidharan R, *et al.* 3D black g-C_3N_4 isotype heterojunction hydrogels as a sustainable photocatalyst for tetracycline degradation and H_2O_2 production. *Chem Eng J* 2023, **475**: 146163.
[22] Dou K, Peng CY, Wang RC, *et al.* S-scheme tubular g-C_3N_4/BiOI heterojunctions for boosting photodegradation of tetracycline and C r(VI): Mechanism insight, degradation pathway and DFT calculation. *Chem Eng J* 2023, **455**: 140813.
[23] Li XF, Qiu YL, Zhu ZL, *et al.* Novel recyclable Z-scheme g-C_3N_4/carbon nanotubes/$Bi_{25}FeO_{40}$ heterostructure with enhanced visible-light photocatalytic performance towards tetracycline degradation. *Chem Eng J* 2022, **429**: 132130.
[24] Vinesh V, Preeyanghaa M, Naveen Kumar TR, *et al.* Revealing the stability of $CuWO_4$/g-C_3N_4 nanocomposite for photocatalytic tetracycline degradation from the aqueous environment and DFT analysis. *Environ Res* 2022, **207**: 112112.
[25] Deng YL, Huang RH, Li X, *et al.* Surfactants modulating of $BiVO_4$ on photocatalytic property as a regulation of surface free energy. *Langmuir* 2024, **40**: 26540–26550.
[26] Zhang XJ, Han DF, Dai MJ, *et al.* Enhanced photocatalytic degradation of tetracycline by constructing a controllable Cu_2O–TiO_2 heterojunction with specific crystal facets. *Catal Sci Technol* 2021, **11**: 6248–6256.
[27] Zhong LL, Chen LY, Xie XL, *et al.* Synthesis of ZnPc/$BiVO_4$ Z-scheme heterojunction for enhanced photocatalytic degradation of tetracycline under visible light irradiation. *Catalysts* 2024, **14**: 722.
[28] Wu SQ, Li XY, Tian YQ, *et al.* Excellent photocatalytic degradation of tetracycline over black anatase-TiO_2 under visible light. *Chem Eng J* 2021, **406**: 126747.
[29] Liu K, Ran MJ, Li ZR, *et al.* CdS QDs grown on ellipsoidal $BiVO_4$ for efficient photocatalytic degradation of tetracycline. *Dalton T* 2024, **53**: 8011–8019.
[30] Hao PC, Shi R, Wang XH, *et al.* Efficient tetracycline degradation using carbon quantum dot modified TiO_2@$LaFeO_3$ hollow core shell photocatalysts. *Sci Rep* 2024, **14**: 27057.
[31] Xia TT, Lu LZ, Zhang HY, *et al.* Inducing piezoelectricity in distorted rutile TiO_2 for enhanced tetracycline hydrochloride degradation through photopiezocatalysis. *J Adv Ceram* 2024, **13**: 323–331.
[32] Liu YB, Li X, Zheng WT, *et al.* Selective reductive degradation of tetracycline via nitrogen-doped copper nanowire networks: Mechanistic insights and pathway elucidation. *ACS EST Eng* 2025, **5**: 2118–2126.
[33] Li F, Wei JH, Wang DB, *et al.* Ce-doped $CuCoO_2$ delafossite with switchable PMS activation pathway for tetracycline degradation. *Chem Eng J* 2024, **481**: 148633.
[34] Wang T, Xue L, Liu YH, *et al.* Insight into the significant contribution of intrinsic defects of carbon-based materials for the efficient removal of tetracycline antibiotics. *Chem Eng J* 2022, **435**: 134822.
[35] Gao WH, Li G, Wang QW, *et al.* Ultrathin porous Bi_2WO_6 with rich oxygen vacancies for promoted adsorption-photocatalytic tetracycline degradation. *Chem Eng J* 2023, **464**: 142694.
[36] Ma H, Ye XY, Li XN, *et al.* Ferroelectric polarization effects of single-atom catalysts on water oxidation. *Adv Mater* 2025, **37**: 2500285.
[37] Zhu QH, Zhang K, Li DQ, *et al.* Polarization-enhanced photocatalytic activity in non-centrosymmetric materials based photocatalysis: A review. *Chem Eng J* 2021, **426**: 131681.
[38] Lv T, Li JX, Arif N, *et al.* Polarization and external-field enhanced photocatalysis. *Matter* 2022, **5**: 2685–2721.
[39] Cui ZY, Xie ZS, Wang YJ, *et al.* Research progress and prospects of photocatalytic devices with perovskite ferroelectric semiconductors. *Acta Phys Sin-Ch Ed* 2020, **69**: 127706.
[40] Zhen C, Ren ZH, Kang YY, *et al.* $PbTiO_3$ based single-domain ferroelectric photocatalysts for water splitting. *Accounts Mater Res* 2023, **4**: 591–603.
[41] Zhao S, Shen SS, Han L, *et al.* Ferroelectric perovskite $PbTiO_3$ for advanced photocatalysis. *Rare Metals* 2024, **43**: 4038–4055.
[42] Huang J, Kang YY, Liu JN, *et al.* Gradient tungsten-doped Bi_3TiNbO_9 ferroelectric photocatalysts with additional built-in electric field for efficient overall water splitting. *Nat Commun* 2023, **14**: 7948.
[43] Zhang J, Liu Y, Dittrich T, *et al.* Unveiling charge utilization mechanisms in ferroelectric for water splitting. *Nat Commun* 2025, **16**: 1515.
[44] Liu Y, Zhang M, Wang Z, *et al.* Bipolar charge collecting structure enables overall water splitting on ferroelectric photocatalysts. *Nat Commun* 2022, **13**: 4245.
[45] Jia GR, Sun FS, Zhou T, *et al.* Charge redistribution of a spatially differentiated ferroelectric $Bi_4Ti_3O_{12}$ single crystal for photocatalytic overall water splitting. *Nat Commun* 2024, **15**: 4746.
[46] Zhang DP, Li YX, Wang PF, *et al.* Regulating spin polarization through cationic vacancy defects in $Bi_4Ti_3O_{12}$ for enhanced molecular oxygen activation. *Angew Chem Int Edit* 2023, **135**: 202303807.
[47] Yu HJ, Wei XD, Wang M, *et al.* Macroscopic polarization enhancement boosting piezo-photocatalytic performance via Nb-doping on B-site of $Bi_4Ti_3O_{12}$ nanosheets. *J Adv Ceram* 2024, **13**: 437–446.
[48] Park BH, Kang BS, Bu SD, *et al.* Lanthanum-substituted bismuth titanate for use in non-volatile memories. *Nature* 1999, **401**: 682–684.
[49] Liu LZ, Huang HW, Chen ZS, *et al.* Synergistic polarization engineering on bulk and surface for boosting CO_2 photoreduction. *Angew Chem Int Edit* 2021, **60**: 18303–18308.
[50] He HQ, Yin J, Li YX, *et al.* Size controllable synthesis of single-crystal ferroelectric $Bi_4Ti_3O_{12}$ nanosheet dominated with{001}facets toward enhanced visible-light-driven photocatalytic activities. *Appl Catal B—Environ* 2014, **156–157**: 35–43.
[51] Zhao XX, Yang H, Li SH, *et al.* Synthesis and theoretical study of large-sized $Bi_4Ti_3O_{12}$ square nanosheets with high photocatalytic activity. *Mater Res Bull* 2018, **107**: 180–188.
[52] Chen ZW, Jiang H, Jin WL, *et al.* Enhanced photocatalytic performance over $Bi_4Ti_3O_{12}$ nanosheets with controllable size and exposed{001}facets for Rhodamine B degradation. *Appl Catal B—Environ* 2016, **180**: 698–706.
[53] Wang CY, Chen F, Hu C, *et al.* Efficient piezocatalytic H_2O_2 production of atomic-level thickness $Bi_4Ti_3O_{12}$ nanosheets with surface oxygen vacancy. *Chem Eng J* 2022, **431**: 133930.
[54] Liu LZ, Hu JC, Ma ZY, *et al.* One-dimensional single atom arrays on ferroelectric nanosheets for enhanced CO_2 photoreduction. *Nat Commun* 2024, **15**: 305.
[55] Xiong RZ, Ding XK, Sun YT, *et al.* Ferroelectric/spin dual-polarization promoted photocatalytic CO_2 methanation of Co-doped $SrBi_4Ti_4O_{15}$. *Sep Purif Technol* 2025, **358**: 130469.
[56] Sun SH, Dong Q, Chen ZW. Macroscopic polarization enhancement boosting piezo-photocatalytic performance of $Bi_4Ti_3O_{12}$ via La-doping. *Ceram Int* 2025, **51**: 3846–3856.
[57] Yau CY, Palan R, Tran K, *et al.* Mechanism of polarization enhancement in La-doped $Bi_4Ti_3O_{12}$ films. *Appl Phys Lett* 2005, **86**: 032907.
[58] Shimakawa Y, Kubo Y, Tauchi Y, *et al.* Crystal and electronic structures of $Bi_{4-x}La_xTi_3O_{12}$ ferroelectric materials. *Appl Phys Lett* 2001, **79**: 2791–2793.
[59] Zhong S, Liu LH, Liu GG, *et al.* Piezoelectric polarization promoted separation of photogenerated carriers in $Bi_{3.25}La_{0.75}Ti_3O_{12}$ with different micro-morphologies for efficient elimination of 2,4-dichlorophenol and tetracycline. *J Clean Prod* 2022, **373**: 133644.
[60] Sun SH, Wang X, Chen ZW, *et al.* Piezoelectric enhanced photocatalytic degradation of levofloxacin by La doped $Bi_4Ti_3O_{12}$ nanosheets. *J Water Process Eng* 2024, **65**: 105787.
[61] Xie ZS, Tang XL, Shi JF, *et al.* Excellent piezo-photocatalytic

performance of $Bi_4Ti_3O_{12}$ nanoplates synthesized by molten-salt method. *Nano Energy* 2022, **98**: 107247.
[62] Tang Q, Wu J, Chen XZ, *et al.* Tuning oxygen vacancies in $Bi_4Ti_3O_{12}$ nanosheets to boost piezo-photocatalytic activity. *Nano Energy* 2023, **108**: 108202.
[63] Wang CY, Tu SC, Chen F, *et al.* Asymmetric single-unit-cell layer enriching polar inherent hydroxyls eliminates interlayer electric field shielding effect and *in situ* self-polarize for piezocatalytic water splitting. *Adv Mater* 2025, **37**: 2505592.
[64] Li JP, Li DY, Cheng Y, *et al.* A Cu–Pb hybrid layer architecture as a new structural prototype for high-efficiency 2D double perovskite broadband emitters. *Angew Chem Int Edit* 2025, **64**: 202507375.
[65] Jing QF, Liu ZY, Cheng X, *et al.* Boosting piezo-photocatalytic activity of BiVO4/$BiFeO_3$ heterojunctions through built-in polarization field tailoring carrier transfer performances. *Chem Eng J* 2023, **464**: 142617.
[66] Guo RS, Jin LH, Zhang Y. Piezo-catalysis in $BiFeO_3$@In_2Se_3 heterojunction for high-efficiency uranium removal. *Small* 2024, **20**: 2307946.
[67] Cao LZ, Wang C, Wang H, *et al.* Rationally designed cyclooctatetrathiophene-based porous aromatic frameworks (COTh-PAFs) for efficient photocatalytic hydrogen peroxide production. *Angew Chem Int Edit* 2024, **136**: 202402095.
[68] Wen GB, Ren BH, Wang X, *et al.* Continuous CO_2 electrolysis using a CO_2 exsolution-induced flow cell. *Nat Energy* 2022, **7**: 978–988.
[69] Wang HR, Zhang XL, Hu C, *et al.* Layered perovskite piezoelectric Bi_3TiNbO_9 as a piezo-photocatalyst: Synergistically enhanced catalytic activity and mechanism. *Appl Surf Sci* 2024, **650**: 159214.
[70] Guo RS, Jin LH, Wang HQ, *et al.* High-efficient U(VI) removal from organic wastewater through polarization electric field enhanced photocatalysis with In_2Se_3@Ag_3PO_4 heterojunction. *J Water Process Eng* 2025, **69**: 106690.
[71] Sun S, Ding JJ, Bao J, *et al.* Photocatalytic degradation of gaseous toluene on Fe–TiO_2 under visible light irradiation: A study on the structure, activity and deactivation mechanism. *Appl Surf Sci* 2012, **258**: 5031–5037.
[72] Hu EM, Liu Q, Qian ZS, *et al.* Unveiling mechanistic insight into accelerating oxygen molecule activation by oxygen defects in Co_3O_{4-x}/g-C_3N_4 p-n heterojunction for efficient photo-assisted uranium extraction from seawater. *Small* 2024, **20**: 2403105.
[73] Jin LH, Tang XW, Wei RH, *et al.* $BiFeO_3$(00l)/$LaNiO_3$/Si thin films with enhanced polarization: An all-solution approach. *RSC Adv* 2016, **6**: 78629–78635.
[74] Hu C, Chen F, Wang YG, *et al.* Exceptional cocatalyst-free photo-enhanced piezocatalytic hydrogen evolution of carbon nitride nanosheets from strong in-plane polarization. *Adv Mater* 2021, **33**: 2101751.
[75] Liu Y, Ye S, Xie HC, *et al.* Internal-field-enhanced charge separation in a single-domain ferroelectric $PbTiO_3$ photocatalyst. *Adv Mater* 2020, **32**: 1906513.
[76] Ghoreishian SM, Ranjith KS, Lee H, *et al.* Hierarchical N-doped TiO_2@$Bi_2W_xMo_{1-x}O_6$ core–shell nanofibers for boosting visible-light-driven photocatalytic and photoelectrochemical activities. *J Hazard Mater* 2020, **391**: 122249.
[77] Zhou Q, Zhang LH, Zhang LF, *et al.* *In-situ* constructed 2D/2D $ZnIn_2S_4$/$Bi_4Ti_3O_{12}$ S-scheme heterojunction for degradation of tetracycline: Performance and mechanism insights. *J Hazard Mater* 2022, **438**: 129438.
[78] Wang HJ, Quan X, Xiong QY, *et al.* Enhanced performance of β-cyclodextrin modified Cu_2O nanocomposite for efficient removal of tetracycline and dyes: Synergistic role of adsorption and photocatalysis. *Appl Surf Sci* 2023, **621**: 156735.
[79] Liu JY, Li YF, Liu XD, *et al.* Synthesis of a novel flower-like $Bi_4Ti_3O_{12}$/AgI Z-type heterojunction for efficient photocatalytic removal of tetracycline antibiotic and RhB. *J Water Process Eng* 2024, **67**: 106262.
[80] Tan BH, Fang Y, Chen QL, *et al.* Construction of $Bi_2O_2CO_3$/Ti_3C_2 heterojunctions for enhancing the visible-light photocatalytic activity of tetracycline degradation. *J Colloid Interf Sci* 2021, **601**: 581–593.
[81] Song TT, Meng XY, Wang HY, *et al.* Visible-LED-light-driven photocatalytic activation of peroxydisulfate by magnetic $ZnFe_2O_4$/Ag nanocomposite for efficient tetracycline degradation. *Sep Purif Technol* 2022, **297**: 121474.
[82] Hu ZY, Wang YL, Wang LZ, *et al.* Synthesis of S-type heterostructure π-COF for photocatalytic tetracycline degradation. *Chem Eng J* 2024, **479**: 147534.
[83] Jiang HL, Wang Q, Chen PH, *et al.* Photocatalytic degradation of tetracycline by using a regenerable (Bi)BiOBr/rGO composite. *J Clean Prod* 2022, **339**: 130771.
[84] Liang YL, Feng AC, Al-Dhabi NA, *et al.* Efficient antibiotic tetracycline degradation and toxicity abatement via the perovskite-type $CaFe_xNi_{1-x}O_3$ assisted heterogeneous electro-Fenton system. *Water Res* 2025, **279**: 123432.
[85] Ouyang LF, Ng M, Zhou ZH, *et al.* Manipulating charge dynamics in carbon nitride by carbon dot doping for efficient photocatalysis. *Adv Sci* 2025, **12**: 2417390.
[86] Guo RS, Jin LH, Chen YX, *et al.* Piezo-photocatalysis of S-scheme In_2Se_3@SnSe heterojunctions for highly efficient U(VI) removal and hydrogen production from organic wastewater. *J Environ Chem Eng* 2024, **12**: 114304.